Advanced Energy Materials

ADVANCED ENERGY MATERIALS
www.advenergymat.de

RESEARCH ARTICLE OPEN ACCESS

Aqueous Lithium Hydroxide Chemistry Based on Hierarchically Assembled Hydrogenated Borophene/Cobalt-Nickel Compounds for Rechargeable High-Performance Supercapattery

Seunghwan Jo[1] | Ozden Gunes Yildiz[2] | Hyun-Sik Kim[3] | Liting Zhang[1] | Ki Hoon Shin[1] | Seong Hyeok Kwon[1] | Keon Beom Lee[1] | Paul Simon[4] | Umut Aydemir[5,6] | Ghim Wei Ho[7,8,9] | Jung Inn Sohn[1]

[1]Department of Physics, Dongguk University, Seoul, Republic of Korea | [2]Graduate School of Sciences and Engineering, Koç University, Istanbul, Türkiye | [3]Department of Materials Science and Engineering, University of Seoul, Seoul, Republic of Korea | [4]Max-Planck-Institut für Chemische Physik fester Stoffe, Dresden, Germany | [5]Koç University Boron and Advanced Materials Application and Research Center, Istanbul, Türkiye | [6]Department of Chemistry, Koç University, Istanbul, Türkiye | [7]Department of Electrical and Computer Engineering, National University of Singapore, Singapore, Singapore | [8]Centre For Hydrogen Innovations, National University of Singapore, Singapore, Singapore | [9]Department of Materials Science and Engineering, National University of Singapore, Singapore, Singapore

Correspondence: Umut Aydemir (uaydemir@ku.edu.tr) | Ghim Wei Ho (elehgw@nus.edu.sg) | Jung Inn Sohn (junginn.sohn@dongguk.edu)

Received: 14 September 2025 | **Revised:** 2 November 2025 | **Accepted:** 13 November 2025

Keywords: aqueous energy storage | cobalt nickel compound | hydrogenated borophene | lattice oxygen mechanism | lithium hydroxide chemistry

ABSTRACT

Lithium hydroxide (LiOH), recognized for its chemical stability, presents a promising discharge product for safe and efficient electrochemical energy storage. While water-driven protonation is crucial for facilitating LiOH chemistry, the reaction mechanism of LiOH in aqueous electrolytes remains unclear. Here, a hierarchically assembled hydrogenated borophene/cobalt-nickel compound (HB/CoNiC) is synthesized using electrochemical-electrophoretic deposition to investigate aqueous LiOH chemistry. The electrophoretic deposition of reducible HB results in the formation of undercoordinated oxygens near partially reduced CoNi alloy nanoparticles. In bi-salt-in-water electrolytes, HB/CoNiC demonstrated a significantly enhanced specific capacitance of 1102 F g^{-1} at a current density of 1 A g^{-1}, which is a 250% improvement compared to CoNiOOH, due to the pseudocapacitive contributions from lithiation and protonation reactions. Furthermore, HB/CoNiC-based supercapatteries exhibited a remarkably high energy density of 112.5 Wh kg^{-1} at a power density of 40 kW kg^{-1} and a capacitance retention of 95.7% over 10 000 cycles at a current density of 20 A g^{-1}, outperforming state-of-the-art aqueous energy storage devices. Electrochemical measurements, ex-situ characterizations, and computational calculations demonstrate that the oxygen nonbonding states in undercoordinated oxygen atoms act as crucial redox centers in lithiation and protonation processes, facilitating efficient and reversible LiOH chemistry in aqueous electrolytes.

Seunghwan Jo, Ozden Gunes Yildiz, and Hyun-Sik Kim contributed equally to this work.

1 | Introduction

Green energy storage technologies are crucial for addressing the escalating global energy demand and mitigating the intermittency of renewable energy sources, including biomass, solar, tidal, and wind power [1, 2]. Among these technologies, lithium batteries have attracted substantial interest due to their high theoretical energy density, positioning them as promising candidates for fulfilling future energy requirements [3, 4]. However, the formation of unstable discharge products and their challenging delithiation process result in the generation of undesirable and hazardous side reaction products that deteriorate the practical performance of lithium batteries. Lithium hydroxide (LiOH) has emerged as an alternative discharge product due to its high chemical stability and high capacity facilitated by the 4-electron discharge process [5, 6]. The reversible LiOH chemistry is heavily reliant on the protonation and deprotonation processes associated with oxygen redox reactions that utilize water as a protic source [7, 8]. To date, considerable attention has been directed towards the development of oxygen redox catalysts, redox mediators, and water additives in aprotic electrolytes to promote the reversible formation and decomposition of LiOH, thereby enabling efficient and durable lithium energy storage systems [9, 10]. Despite its noteworthy potential as a groundbreaking mechanism for next-generation energy storage technologies, research on the feasibility and applicability of LiOH chemistry in environmentally friendly aqueous electrolytes has been limited and infrequently reported. Moreover, the fundamental mechanism governing oxygen redox reactions linked to protonation and deprotonation in aqueous electrolytes is poorly understood and continues to pose a significant challenge.

Recently, transition metal compounds (TMCs) have emerged as exceptionally promising electrode materials capable of offering superior electrochemical energy storage performance in aqueous electrolytes [11–17]. Protonation and deprotonation processes, crucial for efficient discharging and charging reaction pathways through LiOH chemistry, typically occur alongside the oxygen reduction reaction (ORR) and oxygen evolution reaction (OER) [9, 10]. Thus, it is hypothesized that lattice oxygen redox chemistry in TMC-based electrodes can facilitate protonation and deprotonation under conditions involving a covalent metal-oxygen (M—O) bond and undercoordinated oxygen atoms because, under such conditions, the electron energy of oxygen nonbonding states is higher than that of metals due to the downshift of the metal *d*-band [18–21]. Consequently, developing and constructing TMC materials with viable oxygen nonbonding states, capable of undergoing oxygen redox reactions as well as lithiation-delithiation reactions for effective and reversible LiOH chemistry in aqueous electrolytes, is a critical challenge and an essential strategy.

Hydrogenated borophene (HB), a functionalized variant of borophene, is highly attractive for inducing abundant undercoordinated oxygen atoms in TMCs by modulating M-O covalency and enhancing the lithiation-delithiation kinetics of TMC-based electrodes due to its inherent reducibility and rapid charge transfer capabilities [22–27]. Therefore, this study aims to develop new HB-enriched TMCs that feature abundant undercoordinated oxygen atoms, demonstrating their potential for aqueous electrolyte-based energy storage systems with LiOH chemistry while also advancing our understanding of LiOH chemistry in aqueous electrolytes.

Herein, hierarchically assembled HB/cobalt-nickel compounds (HB/CoNiC) nanosheets were synthesized through a combined electrochemical-electrophoretic deposition process. The HB was interspersed with electrochemically deposited CoNi oxyhydroxides via hydrogen bonding. Additionally, highly reducible HB facilitated the generation of undercoordinated oxygen adjacent to partially reduced CoNi alloy nanoparticles on the amorphous CoNi oxyhydroxides. In a BSIW electrolyte composed of 1 M lithium bis(trifluoromethanesulfonyl) imide (LiTFSI) and 1 M potassium hydroxide (KOH), HB/CoNiC exhibited a superior specific capacitance of 1102 F g^{-1} at a current density of 1 A g^{-1}, compared to CoNiOOH (430 F g^{-1}). The specific capacitance of HB/CoNiC in the BSIW electrolyte surpassed the combined capacitances in separate 1 M LiTFSI and 1 M KOH electrolytes, attributable to additional redox contributions from (de)protonation and (de)lithiation reactions. Using the BSIW electrolyte, the HB/CoNiC-based supercapattery demonstrated an energy density of 112.5 Wh kg^{-1} at a power density of 40 kW kg^{-1} and maintained a capacitance retention of 95.7% over 10 000 cycles at a current density of 20 A g^{-1}.

2 | Results and Discussion

Figures S1 and S2 depict the preparation and morphology of neat HB before its incorporation into heterostructures [28]. The synthetic process of hierarchically assembled HB/CoNiC via electrochemical-electrophoretic deposition, along with the resultant bonding structure, is illustrated in Figure 1a. This process involved the electrochemical deposition of CoNiOOH onto carbon paper, followed by the electrophoretic deposition of HB, driven by hydrogen bonding [24, 25]. Field emission scanning electron microscopy (FE-SEM) and field emission transmission electron microscopy (FE-TEM) reveal the nanosheet morphology of both CoNiOOH and HB/CoNiC, with the latter exhibiting a more pronounced nanosheet structure due to the electrophoretically deposited HB (Figure 1b,c; Figure S3). Energy dispersive X-ray spectroscopy (EDS) images confirm the well-dispersed atomic presence of Co, Ni, O, and B within CoNiOOH and HB/CoNiC (Figure 1c; Figure S3). HR-TEM shows the crystalline structure of HB (cyan) and CoNi alloy metal nanoparticles (yellow) with lattice spacings of 4.36 and 2.03 Å, respectively, overlapping the amorphous CoNiOOH (magenta) (Figure 1d) [24, 25, 29, 30]. In contrast, CoNiOOH exhibits an amorphous structure without a clearly ordered atomic arrangement (Figure S4). XRD analysis identifies broad diffraction peaks at 20.3° and 44.8°, indicative of HB and CoNi alloy with weak crystallinity (Figure 1e). Diffraction peaks at 26.5° and 54.6° are attributed to carbon from the carbon paper electrode. These results confirm that HB/CoNiC was successfully synthesized using the electrochemical-electrophoretic deposition technique, yielding a well-defined heterostructure with integrated nanoscale features.

Physical characterizations were employed to demonstrate the structure of HB. While the HB/CoNiC exhibited a crystal phase with a lattice spacing of 4.36 Å, the bare HB featured an

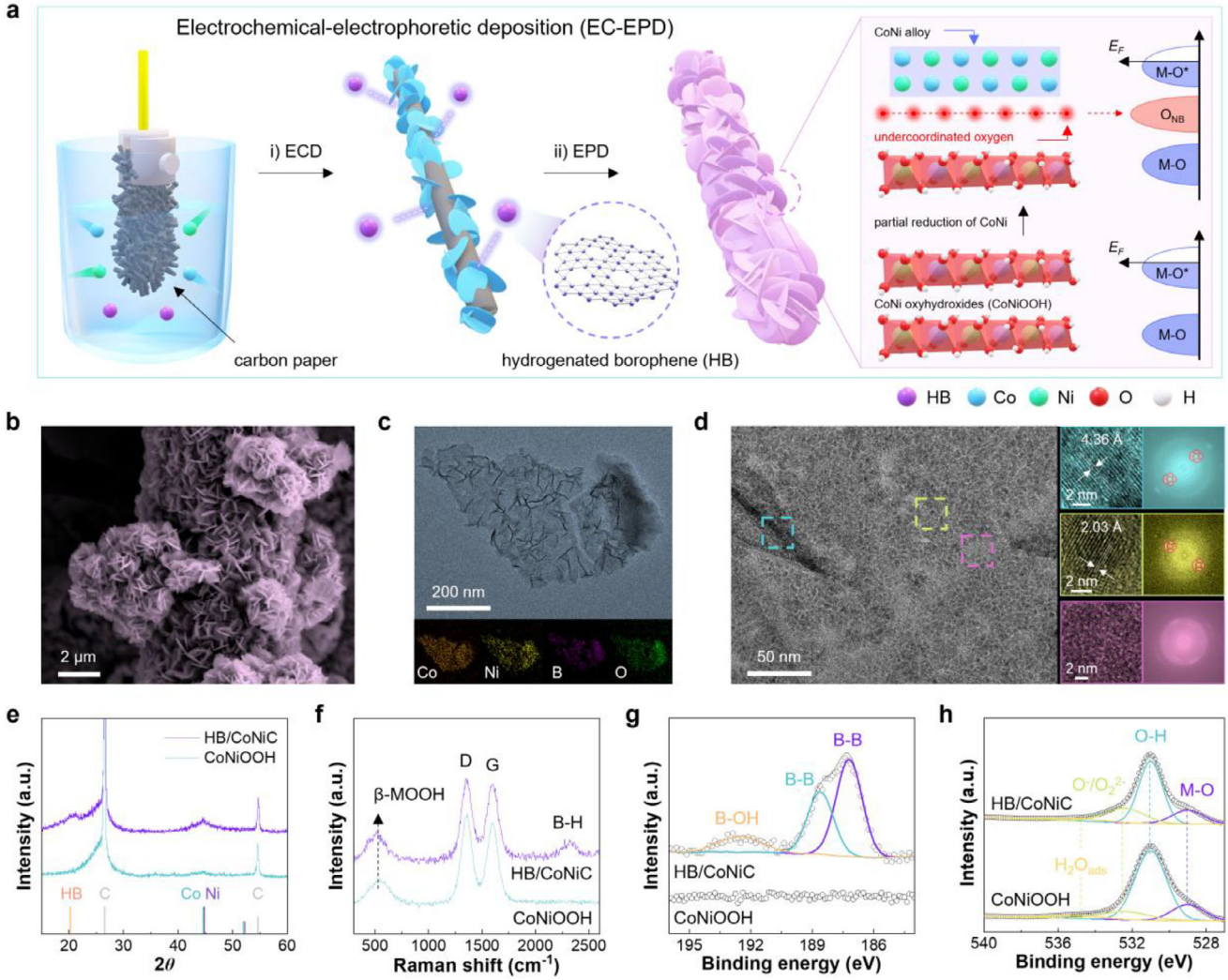

FIGURE 1 | a) Illustration of the electrochemical-electrophoretic deposition process and the electron energy levels of oxygen nonbonding states (O_{NB}). b) Field emission scanning electron microscopy image of HB/CoNiC. c) Field emission transmission electron microscopy (FE-TEM, top) and energy dispersive X-ray spectroscopy (bottom) images of HB/CoNiC. d) High-resolution TEM (left) and magnified TEM images with fast Fourier transform (right) images in three different regions. e) X-ray diffraction patterns and f) Raman spectra. X-ray photoelectron spectroscopy (XPS) spectra in the g) B 1*s* and h) O 1*s* regions.

amorphous structure without a clear ordered arrangement (Figures S2 and S5a). Fourier transform infrared spectroscopy (FT–IR) and X-ray photoelectron spectroscopy (XPS) revealed that the B—OH bonding is additionally observed in the HB/CoNiC due to the adsorbed hydroxide on unsaturated boron sites during the deposition process (Figure S5b,c) [24, 31–33]. These results are attributable to the electrochemical-electrophoretic deposition condition, where abundant hydrogen and hydroxyl sources can adsorb on the surface of HB and rearrange the chemical bonding structure of boron. Raman spectroscopy further confirms the presence of HB. CoNiOOH and HB/CoNiC commonly exhibit broad Raman signals derived from β-phase metal oxyhydroxides (β-MOOH, 520 cm^{-1}) and D and G bands of carbon (1360 and 1610 cm^{-1}) from the carbon paper electrode (Figure 1f) [18, 19]. Additionally, a Raman signal at 2300 cm^{-1}, indicative of the B—H stretching vibration of HB, is confirmed in the HB/CoNiC [24]. Moreover, the B 1*s* XPS spectra identify B—B bonds (187.2 and 188.6 eV) and B-OH (192.5 eV), where the former is attributed to HB and the latter stems from adsorbed hydroxide on unsaturated boron sites during the deposition process (Figure 1g) [24, 31]. In contrast, no Raman or XPS spectra indicate the presence of HB in CoNiOOH.

In the Co 2*p* and Ni 2*p* regions, the XPS spectra of Co^{3+} (779.7 and 794.9 eV), Co^{2+} (781.3 and 796.0 eV), Ni^{2+} (854.4 and 872.0 eV), and Ni^{3+} (856.5 and 874.2 eV) derived from metal oxyhydroxide were observed primarily in CoNiOOH and HB/CoNiC (Figure S6) [34, 35]. Concurrently, metallic Co^0 (778.0 and 793.7 eV) and Ni^0 (852.5 and 869.9 eV) were commonly detected [36, 37]. Nevertheless, the intensities of these zero-valent species were notably higher in HB/CoNiC than in CoNiOOH due to the creation of CoNi alloy metal nanoparticles induced by the addition of reducible HB [22, 23]. In the O 1*s* region, both CoNiOOH and HB/CoNiC exhibited an M—O bond (529.0 eV), an oxygen-hydrogen (O—H) bond (531.0 eV), and oxidized oxygen (O^-/O_2^{2-}) (532.4 eV), where the latter is attributable to an oxygen nonbonding state (Figure 1h) [18–21]. Electron spin resonance (ESR) further revealed that the HB/CoNiC exhibits 6.8 times

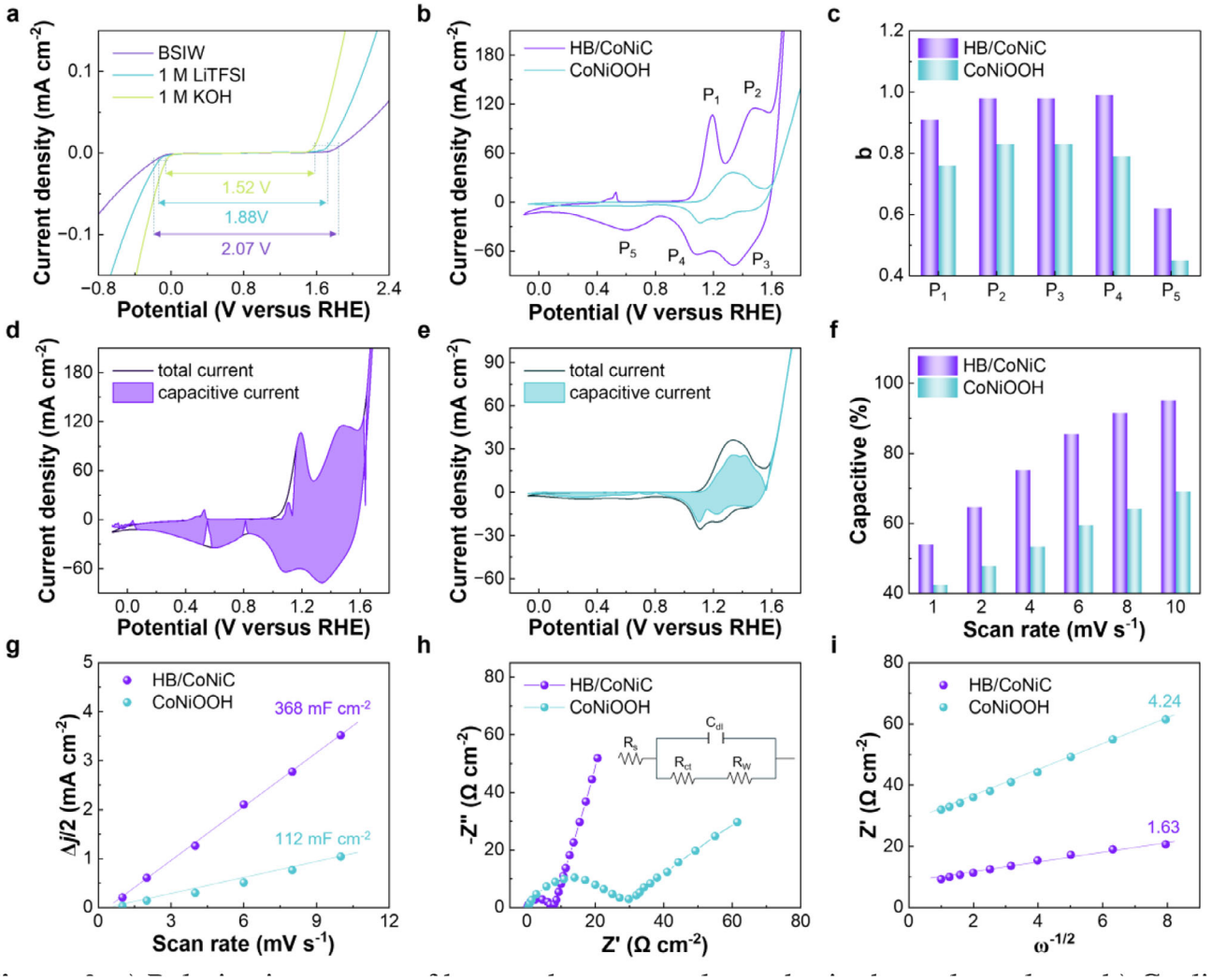

FIGURE 2 | a) Polarization curves of bare carbon paper electrodes in three electrolytes. b) Cyclic voltammetry (CV) curves in bi-salt in water (BSIW) at a scan rate of 10 mV s^{-1}. c) Calculated b values at five redox peaks. The capacitive current density (colored region) of d) HB/CoNiC and e) CoNiOOH at a scan rate of 10 mV s^{-1}. f) The capacitive current densities that contributed to the total current densities with respect to scan rates. g) Double-layer capacitance. h) The Nyquist plots. The inset shows the equivalent circuit of electrochemical impedance spectroscopy (EIS). i) The Warburg impedance coefficient derived from EIS measurements.

higher ESR signal than the CoNiOOH, indicating that the number of lone pair electrons of the oxygen nonbonding state is increased by interaction between HB and the metal (Figure S7). Due to the prevalent oxygen nonbonding state localized around the CoNi alloy metal nanoparticles, HB/CoNiC showed elevated O^-/O_2^{2-} intensity compared to CoNiOOH. These findings suggest that the oxygen redox reaction is facilitated in HB/CoNiC over CoNiOOH, capitalizing on the oxygen nonbonding state (Figure 1a).

The electrochemical performance of CoNiOOH and HB/CoNiC was evaluated in a BSIW electrolyte containing 1 M LiTFSI and 1 M KOH within an expanded potential window (Figure 2a) [36, 37]. The electrochemical potential windows delivering current densities of 0.01 mA cm^{-2} or lower were identified as 1.52, 1.88, and 2.07 V for 1 M KOH, 1 M LiTFSI, and BSIW electrolytes, respectively. In the BSIW electrolyte, HB/CoNiC exhibited distinct oxidation peaks at 1.15 V (P_1) and 1.45 V (P_2) and reduction peaks at 1.35 V (P_3), 1.09 V (P_4), and 0.6–0.8 V (P_5) (Figure 2b). The P_1 oxidation peak was associated with the Faradaic transition reactions from Co^{2+} to Co^{3+}, while the subsequent P_2 peak was attributed to the oxidation reaction from Ni^{2+} to Ni^{3+} [38–40]. Conversely, the P_3 and P_4 reduction peaks indicated the reductive transition reactions of Ni and Co from 3+ to 2+, respectively. Furthermore, the P_5 reduction peak was attributed to oxygen reduction reactions associated with protonation, implying LiOH chemistry [41, 42]. In contrast, CoNiOOH exhibited low current densities with indistinct redox peak shapes, showing minimal evidence of oxygen reduction compared to HB/CoNiC. The power-law analysis revealed that the redox peaks arose from a combination of diffusion-controlled and pseudo-capacitive reactions, with pseudo-capacitive behavior predominantly more significant in HB/CoNiC than in CoNiOOH (Figure 2c).

HB/CoNiC exhibited a predominant pseudo-capacitive contribution (the colored region in the CV curves) of 95.1% of the total current density at a scan rate of 10 mV s^{-1} (Figure 2d). By contrast, CoNiOOH showed a considerably lower pseudo-capacitance contribution of 68.9% at the identical scan rate

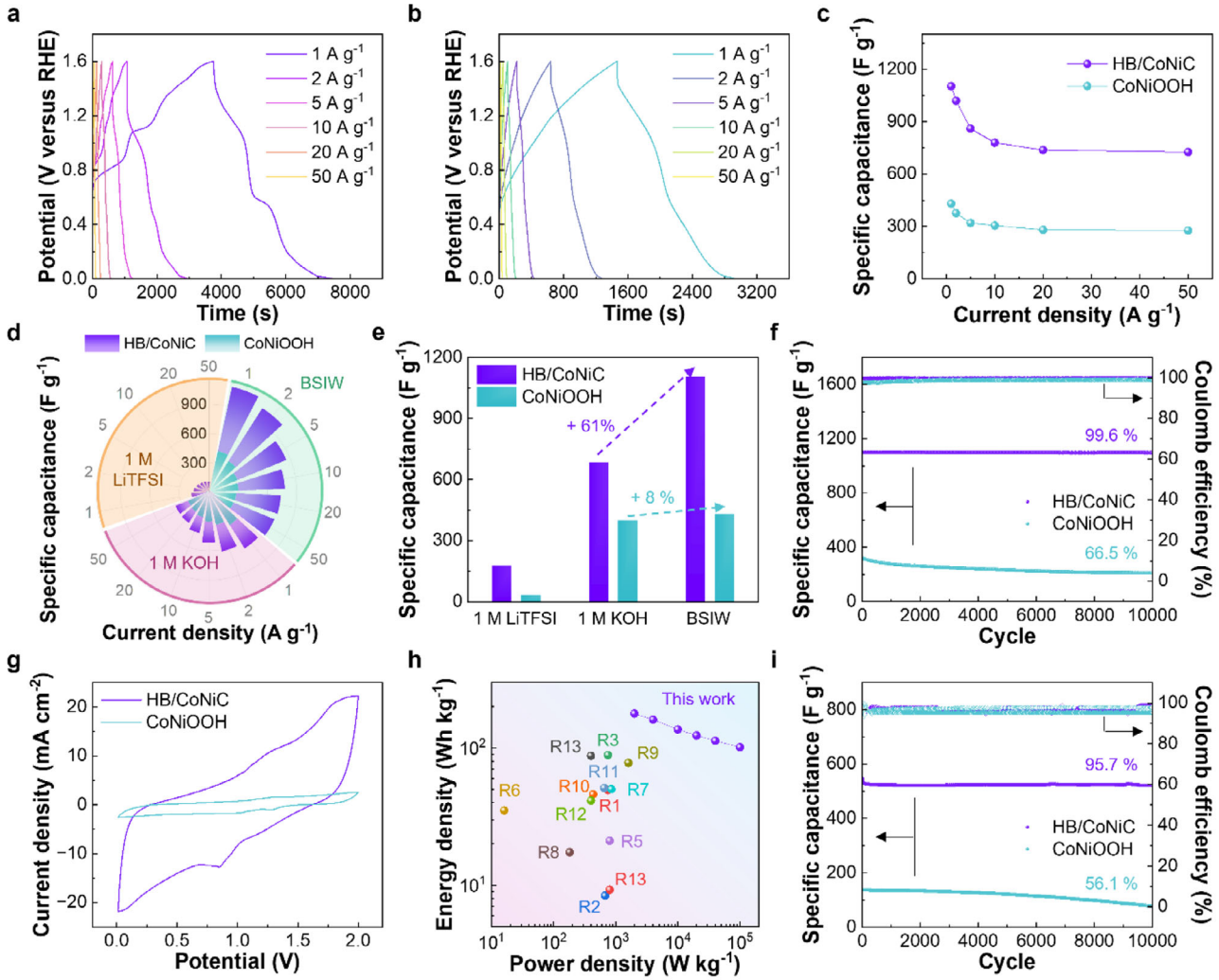

FIGURE 3 | Galvanostatic charge-discharge (GCD) curves of a) HB/CoNiC and b) CoNi oxyhydroxide (CoNiOOH). c) Specific capacitances. d) Wind-rose plots of specific capacitance. e) Specific capacitances at a current density of 1 A g^{-1} in various electrolytes. f) Cycling stability and Coulomb efficiency in BSIW electrolytes. g) CV curves of supercapatteries in BSIW electrolytes. h) Ragone plot comparing the power and energy densities with recently studied energy storage devices. i) Cycling stability and Coulomb efficiency of the supercapatteries.

(Figure 2e). Over scan rates ranging from 1 to 10 mV s^{-1}, HB/CoNiC consistently achieved higher pseudo-capacitive contributions than CoNiOOH (Figure 2f; Figures S8 and S9). In the non-Faradaic potential region, HB/CoNiC attained a superior areal capacitance of 368 mF cm^{-2} compared to CoNiOOH, which reached 112 mF cm^{-2}, suggesting a larger electrochemically active surface area (Figure 2g; Figure S10). The Nyquist plots indicated lower solution and charge transfer resistances for HB/CoNiC (0.15 and 7.6 Ω cm^{-2}) than for CoNiOOH (0.38 and 29.37 Ω cm^{-2}) (Figure 2h). In the low-frequency region, the Warburg coefficients were measured as 1.63 and 4.24 Ω cm^{-2} $s^{-0.5}$ for HB/CoNiC and CoNiOOH, respectively, indicating a significantly reduced ion diffusion resistance in HB/CoNiC (Figure 2i). These findings highlight the superior energy storage performance of HB/CoNiC, attributable to its enhanced pseudo-capacitance and improved ion transport properties.

At current densities ranging from 1 to 50 A g^{-1}, the galvanic charge-discharge (GCD) curves of HB/CoNiC displayed non-linear shapes, indicative of pseudo-capacitance behavior (Figure 3a). Conversely, CoNiOOH exhibited shorter charge-discharge times under identical conditions (Figure 3b). At current densities of 1 and 20 A g^{-1}, HB/CoNiC achieved specific capacitances of 1102 and 737 F g^{-1}, respectively, outperforming CoNiOOH (430 and 278 F g^{-1}) and other recently studied electrodes (Figure 3c; Table S1). The energy storage performance was further evaluated in 1 M KOH and 1 M LiTFSI electrolytes (Figure S11). Wind-rose plots revealed that HB/CoNiC consistently surpassed CoNiOOH across all tested current densities and electrolytes (Figure 3d). CoNiOOH achieved performance in the BSIW electrolyte (430 F g^{-1}), equivalent to 108% of its performance in 1 M KOH (398 F g^{-1}). However, HB/CoNiC exhibited a considerable improvement, achieving a 161% increase in specific capacitance in the BSIW electrolyte (1102 F g^{-1}) compared to 1 M KOH (683 F g^{-1}) at a current density of 1 A g^{-1} (Figure 3e). Additionally, the specific capacitance increased from 33 to 177 F g^{-1} when HB was assembled with CoNiOOH in a 1 M LiTFSI electrolyte at the same current density. Interestingly, the combined specific capacitances in 1 M LiTFSI and 1 M KOH electrolytes for CoNiOOH and HB/CoNiC were

100% and 78%, respectively, of the specific capacitance in the BSIW electrolyte. EIS measurements demonstrated that while the only hydroxide ion transfer governs the energy storage of CoNiOOH, the energy storage of HB/CoNiC stems from the Li and hydroxide ions transfer, enabling synergistically improved energy storage in the BSIW electrolyte (Figure S12). These findings suggest that the significantly enhanced performance of HB/CoNiC in the BSIW electrolyte is attributable to LiOH chemistry.

At a current density of 20 A g^{-1}, cycling stability was assessed over 10 000 cycles to evaluate its practical applicability. HB/CoNiC demonstrated exceptional capacitance retention of 99.6% with nearly 100% Coulomb efficiency, significantly outperforming CoNiOOH, which retained only 66.5% (Figure 3f). To further explore practical applications, supercapattery devices consisting of a pair of electrodes and BSIW electrolytes were fabricated. At a scan rate of 10 mV s^{-1}, the HB/CoNiC-based supercapattery exhibited a significantly higher current density compared to the CoNiOOH-based supercapattery within a potential range of 0–2 V (Figure 3g). Moreover, the HB/CoNiC-based supercapattery also demonstrated superior specific capacitances across current densities ranging from 1 to 50 A g^{-1} (Figure S13). A Ragone plot of power and energy densities indicated that the HB/CoNiC-based supercapattery exhibits a high energy density of 112.5 Wh kg^{-1} at a power density of 40 kW kg^{-1}, which is comparable to, and in some cases superior to, recently studied energy storage devices (Figure 3h; Table S2). Furthermore, during the durability test of 10 000 cycles at a current density of 20 A g^{-1}, the HB/CoNiC-based supercapattery retained 95.7% of its specific capacitance with nearly 100% Coulombic efficiency, significantly outperforming the CoNiOOH-based supercapattery, which retained only 56.1% (Figure 3i).

After the cycling test, FE-SEM confirmed that the morphology of HB/CoNiC was well-maintained (Figure S14). In addition, the crystalline HB and CoNi alloy were well-maintained in the stability-tested HB/CoNiC (Figure S15). The valence states of metal and oxygen in HB/CoNiC were investigated using ex-situ XPS. The XPS spectra revealed that the valence state of metal cations (Co^{3+} and Ni^{3+}) in HB/CoNiC gradually increased during charging and progressively decreased during discharging (Figure 4a; Figure S16). Notably, the metal redox was followed by the oxygen redox, indicating lattice oxygen chemistry driven by the covalent M-O and undercoordinated oxygen [43–45]. It was clearly observed that the intensities of O^-/O_2^{2-} increased and decreased in the fully charged and discharged states, respectively, in the O 1s XPS spectra, which are indicative of lattice oxygen oxidation and reduction [18–21]. In addition, the HB/CoNiC was collected at the various potentials to track the reaction intermediates using a time-of-flight secondary ion mass spectrometry (TOF-SIMS) to further investigate the proposed reaction mechanism. While OH in HB/CoNiC was gradually oxidized into O and dimerized (OO) as the potential increases from R_1 to R_3, Li_2O_2 and LiOH were formed by lithiation and subsequent protonation of OO at potentials R_4 and R_5, respectively (Figure S17). Furthermore, Li_2O_2 was completely transformed into LiOH at the end of discharge, and LiOH was decomposed into hydroxide at potential R_6 as the second cycle started. These results demonstrate the 4-electron transfer reaction pathway between LiOH and OO, mediating O and Li_2O_2 for charge and discharge, respectively, and that the LiOH formation and decomposition reactions are reversible. Furthermore, ^{7}Li nuclear magnetic resonance (NMR) spectra identified the emergence and vanishment of a LiOH signal (1.1 ppm) and a broad signal at the chemical shift of 2140 ppm, attributable to a Fermi contact shift driven by the unpaired electron spin density in amorphous bonding structure around surface-adsorbed Li (Figure 4b) [46, 47]. Simultaneously, Li 1*s* XPS spectra confirmed the formation and decomposition of LiOH (54.8 eV) in the fully discharged and charged states, respectively, demonstrating the reversible LiOH chemistry (Figure 4c) [36, 37]. In contrast, CoNiOOH showed negligible differences in NMR and XPS spectra during the charge-discharge process, and no lithiation-driven products were detected in its discharge state (Figure S18).

Raman spectroscopy identified the E_g bending vibration (δ(M-O), 472 cm^{-1}) and A_{1g} stretching vibration (ν(M-O), 546 cm^{-1}) modes of the γ phase metal oxyhydroxide (γ-MOOH) and peroxo-like oxygen species (M-$(OO)^-$, 1008 cm^{-1}) within the fully charged state of HB/CoNiC (Figure 4d; Figure S19) [18, 19, 21]. While γ-MOOH is related to the oxidized metal cation, M-$(OO)^-$ is attributed to the coupling of undercoordinated oxygen atoms. These results indicate that the downshift of the metal *d*-band below the oxygen nonbonding state can activate oxygen atoms as redox centers, thereby facilitating the coupling of undercoordinated oxygen atoms by utilizing holes in the oxygen nonbonding states [18–21]. Furthermore, the discharged HB/CoNiC exhibited Raman signals attributed to β-MOOH (520 cm^{-1}) and A_{1g} and E_g vibration of LiOH (330 and 620 cm^{-1}), derived from the reduction of metal cations and oxygen anion, illustrating the reversible redox reaction associated with LiOH formation and decomposition [5, 6, 18, 19, 46, 47]. It was revealed that after the cycling test, the signal of the B-H stretching vibration of HB remains constant without significant degradation or structural change (Figure S19). These results indicate that the stable HB in the hierarchically assembled heterostructure facilitates rapid charge transfer to the active sites during the long-term cycling test, eventually enabling reversible LiOH chemistry.

Based on these electrochemical and analytical results, we propose a LiOH-based energy storage mechanism for HB/CoNiC in the BSIW electrolyte (Figure 4e). During the discharge process, metal reduction (P_3 and P_4 regions in CV) and subsequent oxygen reduction (P_5 region in CV) promote LiOH formation via lithiation and protonation, which involve the reduction of undercoordinated oxygen atoms, similar to LiOH formation in aprotic electrolytes (Figure 2b) [5–8]. In the charging process, the decomposition of LiOH involves metal oxidation (P_1 and P_2 regions in CV) and subsequent oxygen oxidation, producing dimerized undercoordinated oxygen atoms (OO). As a metal *d*-band downshift driven by the metal cation oxidation, oxygen nonbonding states in undercoordinated oxygen atoms are positioned higher than those of the metal (high M-O covalency), thereby facilitating the oxidation of undercoordinated oxygen atoms, akin to lattice oxygen redox chemistry [18–21]. Concurrently, the energy storage mechanism varies in 1 M KOH and 1 M LiTFSI electrolytes due to the absence of Li-ion and a deficiency of OH^-, which diminishes proton transfer in alkaline media. Therefore, the synergistic interaction between undercoordinated oxygen and the BSIW electrolyte is essential

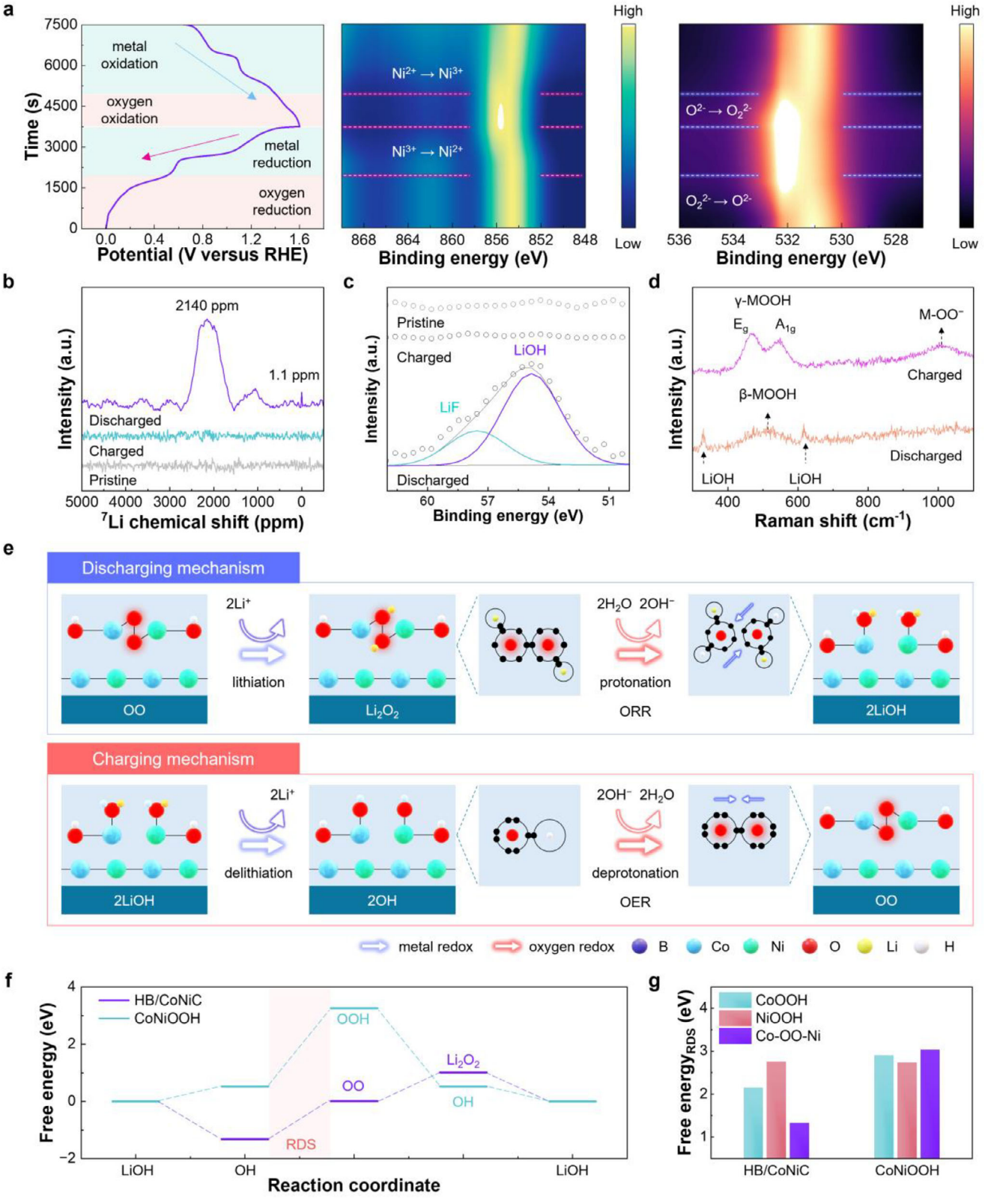

FIGURE 4 | a) Electrochemical curves and Ni 2*p* and O 1*s* XPS spectra of HB/CoNiC during the GCD process. b) ^{7}Li nuclear magnetic resonance, c) Li 1*s* XPS, and d) Raman spectra of cycling stability tested HB/CoNiC. e) Proposed energy storage mechanism of lithium hydroxide chemistry in aqueous electrolyte. f) Free energy diagram of reaction coordinate comprising two-electron transfer steps. g) Free energy differences of rate-determining steps (RDS) based on redox active sites.

for transporting H^+ and Li^+ ions to redox-active oxygens, thereby enabling effective and reversible LiOH chemistry in aqueous conditions.

Density functional theory (DFT) calculations further investigated the proposed catalytic energy storage mechanism. Based on the characterization and electrochemical measurements, the reaction coordinates were analyzed using the cubic CoNi (111)/trigonal CoNiOOH (100) heterostructure and the trigonal CoNiOOH (100) models (Figure S20). It was found that the metal and undercoordinated oxygen can serve as active sites for OOH and OO coordination reaction steps based on the lattice oxygen redox chemistry, leading to distinct reaction pathways. Compared to the OOH pathway, the OO pathway involves the oxygen redox reaction during protonation and deprotonation, and the peroxo-like OO coordination facilitates Li_2O_2 coordination during discharge, analogous to LiOH chemistry [5–8]. Furthermore, the free energy diagrams of LiOH chemistry confirmed that OOH and OO coordination reactions exhibit the largest uphill free energy difference among all the reactions, indicating the rate-determining step (RDS) (Figure 4f). The CoNi/CoNiOOH heterostructure requires a lower free energy of 1.33 eV for the RDS in the OO coordination pathway compared to CoOOH (2.16 eV) and NiOOH (2.73 eV) coordination pathways, demonstrating that the lattice oxygen redox effectively mediates LiOH chemistry (Figure 4g). Meanwhile, CoOOH (2.91 eV) and NiOOH (2.76 eV) are thermodynamically favorable than the OO coordination pathway (3.03 eV) in the CoNiOOH structure, hindering LiOH chemistry in the electrochemical potential window of BSIW. Combining experimental and computational results, we propose an energy storage mechanism in the HB/CoNiC model involving undercoordinated oxygens, enabling lattice oxygen redox to mediate LiOH chemistry in aqueous electrolyte (Figure 4e).

3 | Conclusion

To demonstrate LiOH chemistry within an aqueous electrolyte, the hierarchically assembled HB/CoNiC was synthesized using electrochemical-electrophoretic deposition for supercapattery applications. Incorporating reducible HB facilitated the production of partially reduced CoNi alloy nanoparticles and undercoordinated oxygen atoms, leading to numerous oxygen nonbonding states. HB/CoNiC exhibited an exceptional specific capacitance of 1102 F g^{-1} at a current density of 1 A g^{-1} in a BSIW electrolyte comprising 1 M LiTFSI and 1 M KOH. Additionally, a symmetric HB/CoNiC-based supercapattery demonstrated a high energy density of 112.5 Wh kg^{-1} at a power density of 40 kW kg^{-1} and maintained 95.7% of its specific capacitance after 10,000 cycles at a current density of 20 A g^{-1}. The electrochemical measurements, ex-situ characterizations, and computational calculations confirmed that the enhanced energy storage performance originated from (de)protonation and (de)lithiation reactions. Undercoordinated oxygen atoms with oxygen nonbonding states proved essential for synergizing protonation and deprotonation with ORR and OER to promote LiOH chemistry. These findings offer significant insights into the design of catalytic energy storage materials and the development of aqueous energy storage systems based on LiOH chemistry, highlighting their potential for efficient and durable applications.

4 | Experimental Section

4.1 | Preparation of HB

The HB nanosheet powder was synthesized using an ion-exchange method, as depicted in Figure S1. Initially, MgB_2 polycrystals were prepared via a solid-state synthesis method [28]. Mg and B powders were mixed in a stoichiometric ratio and transferred into a steel ampoule. The ampoule was sealed by arc welding and subsequently annealed under an inert atmosphere, resulting in MgB_2. Following this, 90 mg of MgB_2 powder was dispersed in 300 mL of methanol using a JY92-IIN Scientz ultrasonic probe homogenizer operating at 450 W power in an ice bath for 1 h. Then, 150 mL of methanol suspension containing 45 g of ion-exchange resin (Amberlite IR120, H+ form) was added to the MgB_2 dispersion. The mixture was stirred at 550 rpm under a nitrogen atmosphere for 3 days. Upon completion, the HB powders and methanol solution were separated from the ion-exchange resins via cannula transfer in a closed system under nitrogen, as shown in Figure S1. The obtained methanol-powder mixture was then vacuum-filtered and dried within the same closed system. Lastly, the HB powders were collected in a glovebox to prevent oxidation.

4.2 | Electrochemical-Electrophoretic Deposition

For the preparation of the HB/CoNiC electrode, 2 mM each of cobalt nitrate hexahydrate ($Co(NO_3)_2 \bullet 6H_2O$) and nickel nitrate hexahydrate ($Ni(NO_3)_2 \bullet 6H_2O$), 1 mM of trimesic acid ($C_6H_3(CO_2H)_3$), and 1 mg of HB were added to a mixture consisting of 20 mL of D.I. water and 20 mL of acetonitrile (CH_3CN). Using this suspension as an electrolyte, we conducted electrochemical-electrophoretic deposition at a current density of −80 mA cm^{-2} for 25 min at 40°C in a two-electrode system that included a pair of carbon paper electrodes. The carbon paper was washed with D.I. water and dried in an oven at 60°C after deposition. The exact process was applied to prepare the CoNiOOH electrode, except for adding HB.

4.3 | Characterization

The morphology and atomic configuration of the electrodes were investigated using FE-SEM (ZEISS, Gemini560) and FE-TEM (JEOL, JEM-ARM300F). Elemental mapping images were acquired using an EDS equipped with FE-SEM and FE-TEM systems. The crystal structures of the electrodes were identified using X-ray diffractometry (XRD, Rigaku, Ultima IV). FT-IR (Nicolet 6700, Thermo Scientific) was used to investigate the bonding network. Chemical bonding analyses were performed using Raman spectroscopy (WEVE, HEDA) and XPS (ULVAC-PHI, Versaprobe II). ESR (Bruker, EMXplus-9.5) was used to identify lone-paired electron density. Particle and pore size analysis (PSA) system (UPA-150, ASAP2010, AutoporeIV) was used to measure the Brunauer–Emmett–Teller (BET) surface area. The HB/CoNiC and CoNiOOH exhibited the BET surface areas of 95.90 and 46.87 m^2 g^{-1}, respectively. A solid-state ^{7}Li-NMR spectrometer (Bruker, Avance III HD) acquired NMR spectra through 500 MHz Hahn-echo pulse magic angle spinning experiments with a $\pi/2$ pulse width of 1.0 μs and a relaxation delay of 50 ms. All the acquired

isotopic ^{7}Li spectra were referenced against 1 M LiCl at 0 ppm. The reaction intermediates were investigated using TOF-SIMS (M6, IONTOF GmbH).

Acknowledgements

This research was supported by the National Research Foundation of Korea (NRF), funded by the Ministry of Science and ICT (RS-2024-00344256, RS-2025-24534218). This work was supported by Centre for Hydrogen Innovations (CHI-P2024–08). U.A. and O.G.Y. acknowledge financial support from the Air Force Office of Scientific Research (AFOSR) under award number FA8655-24-1-7389.

Funding

This research was supported by the National Research Foundation of Korea (NRF), funded by the Ministry of Science and ICT (RS-2024-00344256, RS-2025-24534218). U.A. and O.G.Y. acknowledge financial support from the Air Force Office of Scientific Research (AFOSR) under award number FA8655-24-1-7389.

Conflicts of Interest

The authors declare no conflicts of interest.

Data Availability Statement

The data that support the findings of this study are available from the corresponding author upon reasonable request.

References

1. Z. Zhang, T. Ding, Q. Zhou, et al., "A Review of Technologies and Applications on Versatile Energy Storage Systems," *Renewable and Sustainable Energy Reviews* 148 (2021): 111263, https://www.sciencedirect.com/science/article/pii/S1364032121005505.

2. K. M. Tan, T. S. Babu, V. K. Ramachandaramurthy, P. Kasinathan, S. G. Solanki, and S. K. Raveendran, "Empowering Smart Grid: A Comprehensive Review of Energy Storage Technology and Application with Renewable Energy Integration," *Journal of Energy Storage* 39 (2021): 102591, https://www.sciencedirect.com/science/article/pii/S2352152X21003340.

3. P. Lyu, X. Liu, J. Qu, et al., "Recent Advances of Thermal Safety of Lithium Ion Battery for Energy Storage," *Energy Storage Materials* 31 (2020): 195–220, https://www.sciencedirect.com/science/article/pii/S2405829720302646.

4. X. Fan and C. Wang, "High-Voltage Liquid Electrolytes for Li Batteries: Progress and Perspectives," *Chemical Society Reviews* 50 (2021): 10486–10566, https://pubs.rsc.org/en/content/articlelanding/2021/cs/d1cs00450f.

5. X. Bi, M. Li, C. Liu, et al., "Cation Additive Enabled Rechargeable LiOH-Based Lithium–Oxygen Batteries," *Angewandte Chemie International Edition* 59 (2020): 22978–22982, https://onlinelibrary.wiley.com/doi/full/10.1002/anie.202010745.

6. J. Lu, S. Dey, I. Temprano, et al., "Co 3 O 4 -Catalyzed LiOH Chemistry in Li–O 2 Batteries," *ACS Energy Letters* 5 (2020): 3681–3691, https://pubs.acs.org/doi/full/10.1021/acsenergylett.0c01940.

7. S. Wu, Y. Qiao, S. Yang, M. Ishida, P. He, and H. Zhou, "Organic Hydrogen Peroxide-Driven Low Charge Potentials for High-Performance Lithium-Oxygen Batteries with Carbon Cathodes," *Nature Communications* 8 (2017): 15607, https://www.nature.com/articles/ncomms15607.

8. M. Kim, H. Lee, H. J. Kwon, et al., "Carbon-Free High-Performance Cathode for Solid-State Li-O_2 Battery," *Science Advances* 8 (2022): abm8584, https://www.science.org/doi/full/10.1126/sciadv.abm8584.

9. T. Liu, G. Kim, E. Jónsson, et al., "Understanding LiOH Formation in a Li-O_2 Battery with LiI and H_2O Additives," *ACS Catalysis* 9 (2019): 66–77, https://pubs.acs.org/doi/full/10.1021/acscatal.8b02783.

10. Z. Gao, I. Temprano, J. Lei, et al., "Recent Progress in Developing a LiOH-Based Reversible Nonaqueous Lithium–Air Battery," *Advanced Materials* 35 (2023): 2201384, https://advanced.onlinelibrary.wiley.com/doi/full/10.1002/adma.202201384.

11. Y. Li, J. Zhang, Q. Chen, X. Xia, and M. Chen, "Emerging of Heterostructure Materials in Energy Storage: A Review," *Advanced Materials* 33 (2021): 2100855, https://advanced.onlinelibrary.wiley.com/doi/full/10.1002/adma.202100855.

12. Q. Dou, N. Wu, H. Yuan, et al., "Emerging Trends in Anion Storage Materials for the Capacitive and Hybrid Energy Storage and beyond," *Energy Environmental Science* 50 (2021): 6734–6789, https://pubs.rsc.org/en/content/articlehtml/2021/cs/d0cs00721h.

13. X. Zhao, L. Mao, Q. Cheng, et al., "Two-Dimensional Spinel Structured Co-Based Materials for High Performance Supercapacitors: A Critical Review," *Chemical Engineering Journal* 387 (2020): 124081, https://doi.org/10.1016/j.cej.2020.124081.

14. W. Xu, X. Zhao, F. Zhan, et al., "Toward Emerging Two-dimensional Nickel-based Materials for Electrochemical Energy Storage: Progress and Perspectives," *Energy Storage Materials* 53 (2022): 79–135, https://doi.org/10.1016/j.ensm.2022.08.039.

15. J. Chen, W. Xu, H. Wang, et al., "Emerging Two-Dimensional Nanostructured Manganese-based Materials for Electrochemical Energy Storage: Recent Advances, Mechanisms, Challenges, and Prospects," *Journal of Materials Chemistry A* 10 (2022): 21197–21250, https://doi.org/10.1039/D2TA05309H.

16. Y. Qian, Q. Ruan, M. Xue, and L. Chen, "Emerging Perovskite Materials for Supercapacitors: Structure, Synthesis, Modification, Advanced Characterization, Theoretical Calculation and Electrochemical Performance," *Journal of Energy Chemistry* 89 (2024): 41–70, https://doi.org/10.1016/j.jechem.2023.10.028.

17. T. Liu, S. Liu, Y. Liao, L. Sun, J. Bai, and L. Chen, "Two-Dimensional Nanostructures of Transition Metal-Based Materials Towards Aqueous Electrochemical Energy Storage," *Chemical Communications* 61 (2025): 5094–5109, https://doi.org/10.1039/D4CC06341D.

18. Z.-F. Huang, J. Song, Y. Du, et al., "Chemical and Structural Origin of Lattice Oxygen Oxidation in Co–Zn Oxyhydroxide Oxygen Evolution Electrocatalysts," *Nature Energy* 4 (2019): 329–338, https://www.nature.com/articles/s41560-019-0355-9.

19. X. Wang, H. Zhong, S. Xi, W. S. V. Lee, and J. Xue, "Understanding of Oxygen Redox in the Oxygen Evolution Reaction," *Advanced Materials* 34 (2022): 2107956, https://advanced.onlinelibrary.wiley.com/doi/full/10.1002/adma.202107956.

20. S. Jo, W. B. Park, K. B. Lee, et al., "Bi/BiFe(oxy)Hydroxide for Sustainable Lattice Oxygen-boosted Electrocatalysis at a Practical High Current Density," *Applied Catalysis B: Environmental* 317 (2022): 121685, https://www.sciencedirect.com/science/article/pii/S0926337322006269.

21. S. Jo, J. I. Jeon, K. H. Shin, et al., "Stabilization of Lattice Oxygen Evolution Reactions in Oxophilic Ce-Mediated Bi/BiCeO 1.8 H Electrocatalysts for Efficient Anion Exchange Membrane Water Electrolyzers," *Advanced Materials* 36 (2024): 2314211, https://advanced.onlinelibrary.wiley.com/doi/full/10.1002/adma.202314211.

22. S. Gao, Y. Zhang, J. Bi, et al., "2D hydrogenated Boride as a Reductant and Stabilizer for In Situ Synthesis of Ultrafine and Surfactant-Free Carbon Supported Noble Metal Electrocatalysts with Enhanced Activity and Stability," *Journal of Materials Chemistry A* 8 (2020): 18856–18862, https://pubs.rsc.org/en/content/articlehtml/2003/pw/d0ta06542k.

23. X. Zeng, Y. Jing, S. Gao, et al., "Hydrogenated Borophene Enabled Synthesis of Multielement Intermetallic Catalysts," *Nature Communications* 14 (2023): 7414, https://www.nature.com/articles/s41467-023-43294-z.

24. C. Hou, G. Tai, J. Hao, L. Sheng, B.o Liu, and Z. Wu, "Ultrastable Crystalline Semiconducting Hydrogenated Borophene," *Angewandte Chemie*

International Edition 59 (2020): 10819–10825, https://onlinelibrary.wiley.com/doi/full/10.1002/anie.202001045.

25. Q. Li, V. S. C. Kolluru, M. S. Rahn, et al., "Synthesis of Borophane Polymorphs Through Hydrogenation of Borophene," *Science* 371 (2021): 1143–1148, https://www.science.org/doi/full/10.1126/science.abg1874.

26. O. G. Yildiz and U. Aydemir, "Borophene: Challenges in Stability and Pathways to Synthesis," *Materials Science and Engineering: R: Reports* 163 (2025): 100913, https://www.sciencedirect.com/science/article/pii/S0927796X24001438.

27. O. G. Yildiz, A. C. Can, N. S. Peighambardoust, and U. Aydemir, "From Synthesis to Functionality: Borophene's Transformative Potential in Next-Generation Electrocatalysis and Battery Applications," *Small Structures* 6 (2025): 2500186, https://doi.org/10.1002/sstr.202500186.

28. E. Sadeghi, N. S. Peighambardoust, M. Khatamian, U. Unal, and U. Aydemir, "Metal Doped Layered MgB_2 Nanoparticles as Novel Electrocatalysts for Water Splitting," *Scientific Reports* 11 (2021): 3337, https://www.nature.com/articles/s41598-021-83066-7.

29. Y. Tan, Z. Zhang, Z. Lei, et al., "Electronic Modulation Optimizes OH* Intermediate Adsorption on Co-Nx-C Sites via Coupling CoNi Alloy in Hollow Carbon Nanopolyhedron Toward Efficient Reversible Oxygen Electrocatalysis," *Applied Catalysis B: Environmental* 304 (2022): 121006, https://www.sciencedirect.com/science/article/pii/S0926337321011310.

30. J. Li, X. Wang, C. Jian, et al., "GO-CoNi Alloy Promotes Internal Reaction Kinetics of Lithium-Sulfur Batteries to Improve Long Cycle Performance at High-Rate," *Chemical Engineering Journal* 474 (2023): 145994, https://www.sciencedirect.com/science/article/pii/S1385894723047253.

31. X. Wang, J. Liang, Q. You, et al., "Bandgap Engineering of Hydroxy-Functionalized Borophene for Superior Photo-Electrochemical Performance," *Angewandte Chemie International Edition* 59 (2020): 23559–23563, https://onlinelibrary.wiley.com/doi/full/10.1002/anie.202010723.

32. K. Zielinkiewicz, D. Baranowska, and E. Mijowska, "Ball Milling Induced Borophene Flakes Fabrication," *RSC Advances* 13 (2023): 16907–16914. https://doi.org/10.1039/D3RA02400H.

33. O. G. Yildiz and U. Aydemir, "Beyond Graphene: Hydrogenated Borophene as a Next-Generation Adsorbent for Ultra-Fast Water Purification," *Separation and Purification Technology* 377 (2025): 134213, https://doi.org/10.1016/j.seppur.2025.134213.

34. S. Jo, K. B. Lee, and J. I. Sohn, "Direct Electrosynthesis of Selective Transition-Metal Chalcogenides as Functional Catalysts with a Tunable Activity for Efficient Water Electrolysis," *ACS Sustainable Chemistry & Engineering* 9 (2021): 14911–14917, https://pubs.acs.org/doi/full/10.1021/acssuschemeng.1c05130.

35. S. Jo, M.-C. Kim, K. B. Lee, H. Choi, L. Zhang, and J. I. Sohn, "Nonprecious High-Entropy Chalcogenide Glasses-Based Electrocatalysts for Efficient and Stable Acidic Oxygen Evolution Reaction in Proton Exchange Membrane Water Electrolysis," *Advanced Energy Materials* 13 (2023): 2301420, https://advanced.onlinelibrary.wiley.com/doi/full/10.1002/aenm.202301420.

36. J. Zhang, C. Cui, P.-F. Wang, et al., ""Water-In-Salt" Polymer Electrolyte for Li-Ion Batteries," *Energy & Environmental Science* 13 (2020): 2878–2887, https://pubs.rsc.org/en/content/articlehtml/2019/7d/d0ee01510e.

37. J. Xu, X. Ji, J. Zhang, et al., "Aqueous Electrolyte Design for Super-Stable 2.5 V LiMn2O4 || Li4Ti5O12 Pouch Cells," *Nature Energy* 7 (2022): 186–193, https://www.nature.com/articles/s41560-021-00977-5.

38. B. Huang, H. Wang, S. Liang, et al., "Two-Dimensional Porous Cobalt–Nickel Tungstate Thin Sheets for High Performance Supercapattery," *Energy Storage Materials* 32 (2020): 105–114, https://doi.org/10.1016/j.ensm.2020.07.014.

39. A. De La Fuente Durán, A. Y.-L. Liang, I. Denti, et al., "Origins of Hydrogen Peroxide Selectivity During Oxygen Reduction on Organic Mixed Ionic–Electronic Conducting Polymers," *Energy & Environmental Science* 16 (2023): 5409–5422, https://pubs.rsc.org/en/content/articlehtml/2023/ee/d3ee02102e.

40. B.-H. Lee, H. Shin, A. S. Rasouli, et al., "Supramolecular Tuning of Supported Metal Phthalocyanine Catalysts for Hydrogen Peroxide Electrosynthesis," *Nature Catalysis* 6 (2023): 234–243, https://www.nature.com/articles/s41929-023-00924-5.

41. B. Li, Z. Zhuo, L. Zhang, et al., "Decoupling the Roles of Ni and Co in Anionic Redox Activity of Li-Rich NMC Cathodes," *Nature Materials* 22 (2023): 1370–1379, https://www.nature.com/articles/s41563-023-01679-x.

42. X. Gao, B. Li, K. Kummer, et al., "Clarifying the Origin of Molecular O_2 in Cathode Oxides," *Nature Materials* 24 (2025): 743–752, https://www.nature.com/articles/s41563-025-02144-7.

43. J. H. Yu, K. Koster, N. Voronina, et al., "Elevating Li-Ion Battery Paradigms: Sophisticated Ionic Architectures in Lithium-Excess Layered Oxides for Unprecedented Electrochemical Performance," *eScience* 5 (2025): 100376, https://www.sciencedirect.com/science/article/pii/S2667141725000060.

44. E. N. Bassey, P. J. Reeves, I. D. Seymour, and C. P. Grey, "^{17}O NMR Spectroscopy in Lithium-Ion Battery Cathode Materials: Challenges and Interpretation," *Journal of the American Chemical Society* 144 (2022): 18714–18729, https://pubs.acs.org/doi/full/10.1021/jacs.2c02927.

45. J. Lei, Z. Gao, L. Tang, et al., "Coupling Water-proof Li Anodes with LiOH-Based Cathodes Enables Highly Rechargeable Lithium–Air Batteries Operating in Ambient Air," *Advanced Science* 9, no. 4 (2022): 2103760, https://advanced.onlinelibrary.wiley.com/doi/full/10.1002/advs.202103760

46. G. Leverick, Y. G. Zhu, S. Lohmar, F. Bardé, S. Cotte, and Y. Shao-Horn, "Six-Electron Reduction of $LiIO_3$ to LiOH in Aprotic Solvents and Implications for Li–O_2 Batteries," *The Journal of Physical Chemistry C* 126, no. 19 (2022): 8256–8267, https://pubs.acs.org/doi/full/10.1021/acs.jpcc.2c01888.

47. L.-N. Song, X.-X. Wang, H.-F. Wang, et al., "Dual Active Intermediates Induced LiOH Formation via the OH-Rich Proton Donor in Li–O 2 Batteries," *Advanced Functional Materials* 35 (2025): 2414854, https://advanced.onlinelibrary.wiley.com/doi/full/10.1002/adfm.202414854.

Supporting Information

Additional supporting information can be found online in the Supporting Information section.

Supporting file: aenm70467-sup-0001-SuppMat.docx